

Reviewer #1:

Reply: We revised the manuscript according to your reviewing. Following are the point-by-point response to reviewer #1 comments for specifying all changes in the mark-up manuscript.

1. Line 26 (and 357): Statement “The results show that 27 different types of currents” is confusing, as it implies there are 27 categories of currents this study uncovered. I am guessing authors meant that this study investigated 27 cases with carrying winds, waves, and currents.

Previous Author’s Reply: We revised the sentences in lines 26 and 357 in the manuscript.

Change in Manuscript: We revised the sentences in lines 26-28 in the mark-up manuscript. We revised the sentences in lines 398-400 in the mark-up manuscript.

2. Line 44-45: maximum ocean surface current velocity is certainly more than 1 m/s.

Previous Author’s Reply: We revised the sentence in line 46 in the manuscript.

Change in Manuscript: We revised the sentences in lines 46-47 in the mark-up manuscript.

3. Introduction: Other than the high winds and the lack of data, the introduction seems to be missing a scientific objective or a hypothesis. Please elaborate what reasons did the authors have to doubt that waves might not follow the dispersion relationship in high winds. Why wouldn’t they?

Previous Author’s Reply: Wind waves follow the dispersion relationship at normal wind speeds. At extremely high wind speeds, the water surface is intensively broken because of strong surface wind shear (e.g. Donelan et al., 2004; Troitskaya et al., 2012, 2017, 2018a, 2018b; Takagaki et al., 2012, 2016; Holthuijsen et al., 2012). Thus, it is unclear if such wind waves with the surface foam layer at extremely high wind speeds have properties similar to those of the wind waves at normal wind speeds. We added a detailed explanation to the introduction of the revised manuscript.

Change in Manuscript: We revised the sentences in lines 54-70 in the mark-up manuscript.

4. Table: How were U_{10} and U^* calculated from the wind speed measurements in the tunnel? This question becomes especially intriguing as wind speed studied here goes far beyond applicability limits of any C_D parameterization.

Previous Author's Reply: The values of U_{10} and u^* taken in Kyoto University (Cases 1-14) were estimated by the eddy correlation method using a laser Doppler anemometer (LDA) at normal wind speeds and a phase Doppler anemometer (PDA) at high wind speeds. The details were written in previous papers by the authors (e.g. Takagaki et al., 2012; Iwano et al., 2013; Komori et al., 2018), where we briefly explain the method: the air velocity and Reynolds stress were measured at a fetch of $x = 6.5$ m using a phase Doppler anemometer (Dantec Dynamics PDA). Laser beams were shot through the plate-glass sidewall, and we prepared a small droplet-adherent prevention device (DAPD) to avoid irregular reflection by the wall and impingement of the droplets dispersed from the intensively breaking wind waves. The DAPD had a size of 0.07 m x 0.07 m x 0.007 m and was fixed on the inside glass wall (Fig. A1). Four orifices with a diameter of 0.005 m were installed on the device, and four laser beams were introduced through the orifices into the test section. Clean, compressed air was blown through the orifices along the plate-glass sidewall. Therefore, even if dispersed droplets impinged on and adhered to the orifices, the compressed air removed the droplets, creating a clear path for the laser beam. As the PDA enabled us to simultaneously measure the diameter (d_p), streamwise and vertical velocities, and number of dispersed droplets, we could measure the streamwise air velocity (U_p) and the product of the streamwise and vertical air velocity fluctuations ($u_p v_p$) by conditionally extracting the signals from dispersed droplets of $d_p < 30$ μm . Thus, we defined the mean velocity (U) and the Reynolds stress ($-uv$) in air as the ensemble averaged values ($\langle U_p \rangle$ and $\langle u_p v_p \rangle$) of U_p and $u_p v_p$ for droplets of $d_p < 30$ μm . The air friction velocity (u^*) was estimated by an eddy correlation method as $u^* = (-\langle u_p v_p \rangle)^{1/2}$, because the shear stress at the interface (τ) was defined by $\tau = \rho u^{*2} = \rho C_D U_{10}^2$. The value of $(-\langle u_p v_p \rangle)^{1/2}$ was estimated by extrapolating the measured values of the Reynolds stress to the mean surface $z = 0$ m. The U_{10} was estimated by the log-law: $U_{10} - U_{\min} = u^*/\kappa \ln(z_{10}/z_{\min})$, where U_{\min} is the air velocity nearest the water surface (z_{\min}), and z_{10} is 10 m. Moreover, the drag coefficient C_D was estimated by $C_D = (u^*/U_{10})^2$.

The values of U_{10} and u^* taken in Kindai University (Cases 21-27) were estimated by the empirical curve by Iwano et al. (2013), which was proposed by the above eddy correlation method.

The values of U_{10} and u^* taken in IAP RAS (Cases 15-20) were taken from Troitskaya

et al. (2012) by a Pitot tube, where u^* was estimated by a profile method considering the profiles in the constant flux layer and the wake region:

$$U_\infty - U(z) = u^* \left(-\frac{1}{\kappa} \ln(z/\delta) + \alpha \right); z/\delta < 0.15, \quad (A1)$$

$$U_\infty - U(z) = \beta u^* (1 - z/\delta)^2; z/\delta > 0.15, \quad (A2)$$

respectively. Here, U_∞ is the freestream wind speed, δ is the boundary layer thickness; α and β are the constant values that depend on flow fields. The constant values of α and β are calibrated at low wind speeds without the dispersed droplets. Measuring the profile in the constant flux layer (Eq. A1) in extremely high wind speeds is difficult because of the large breaking waves and dispersed droplets. Thus, using β measured at low wind speeds, u^* is estimated by Eq. (A2) at extremely high wind speeds. The value of U_{10} is estimated by Eq. (A1) at $z = 10$ m with α measured at normal wind speeds. The value of C_D is estimated by $\tau = \rho u^{*2} = \rho C_D U_{10}^2$. Although the measurement methods for u^* , U_{10} , and C_D in IAP RAS and Kyoto are different, the values approximately correspond to each other (see Troitskaya et al. (2012) and Takagaki et al. (2012)).

We added these methods for estimating u^* , U_{10} , and C_D in the revised manuscript.

Change in Manuscript: We revised the sentences in lines 104-112, lines 123-136, and lines 151-153 in the mark-up manuscript.

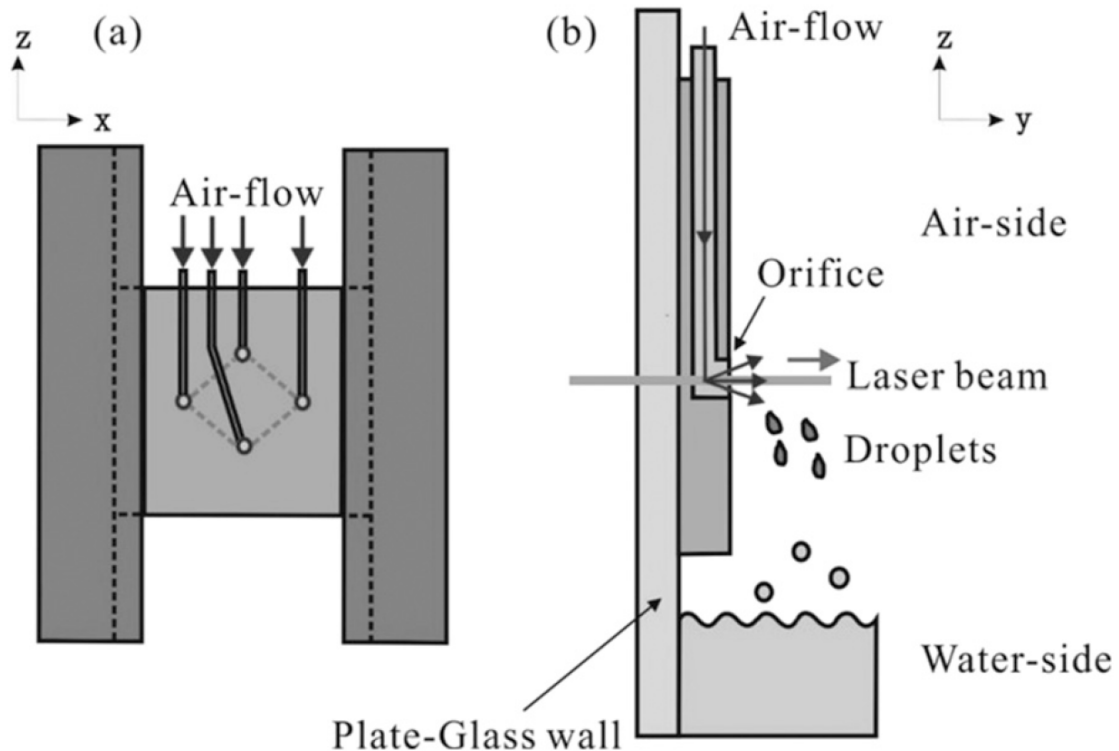


Fig. A1: Droplet-adherent prevention device attached to the plate-glass sidewall. (a) View on the x - z plane and (b) view on the y - z plane; x , y , and z represent the streamwise, spanwise, and vertical directions, respectively. The four circles in (a) indicate the four orifices.

5. Table: What is freestream wind velocity? How is it defined and calculated?

Previous Author's Reply: The freestream wind velocity is the wind velocity in the freestream region, that is, the wind velocity outside the boundary layer, which is the constant velocity. The freestream wind speed is calculated as the average velocity in the freestream region.

Change in Manuscript: We didn't revise any sentences in the mark-up manuscript.

6. Methodology: Paper's conclusions could have been reached based on a single tank experiment. Why use three tanks? Is that because no single tank had all required capabilities (e.g., high wind vs current control, etc.)? Please add an explanation in the methodology section.

Previous Author's Reply: We obtained the conclusion through experiments using three tanks. We observed that wind waves do not follow the dispersion relation at either normal or the

extremely high wind speeds in the three tanks—excluding case 25, which was the artificial current experiment using the Kindai tank (Fig. 4). In case 25, U_{SURF} is approximately zero; thus, the Doppler shift does not occur in this situation, and the results in Fig. 4 were obtained from the three tanks. Then, using 18 datasets (Kyoto and IAP RAS tanks), we found that the ratio of $C_S/C_{S,0}$ is constant at normal and extremely high wind speeds (Fig. 5), implying that the same wave-current interaction occurs at normal and extremely high wind speeds. From the artificial current experiment in Kindai, we observed that the ratio varies (Fig. 5). Thus, the results in Fig. 5 were also obtained with the three tanks. We used 17 datasets—which included current profiles—to investigate the empirical and theoretical model at both normal and extremely high wind speeds (Figs. 6 and 7). Because the explanation in the previous manuscript may mislead readers, we added this detailed explanation, which is equivalent to the methodology, to the conclusion section of the revised manuscript.

Change in Manuscript: We revised the sentences in lines 401-411 in the mark-up manuscript.

7. Lines 98-99 How was the phase speed C_S calculated? Lines 98-99 mentioned some “cospectra method” and refer to Takagaki et al., 2017, but I looked through that article and did not find it. I think this method should be presented in greater detail in this manuscript. It is important to understand if the underlying currents, including the surface drift current, as well as the observed sharp vertical profile, might skew this estimate.

Previous Author’s Reply: We agree with your statement, changed the name to “cross-spectrum method”, and added the explanation in an appendix of the revised manuscript for calculating the phase velocity C_S and wavelength L_S . The following is the explanation.

Cross-spectrum method

The water-level fluctuation $\eta(x, t)$ at an arbitrary location x and time t is shown as the equation:

$$\eta(x, t) = \int_{-\Omega}^{\Omega} A(\omega) e^{i(\omega t - k(\omega)x)} d\omega \quad (\text{A1})$$

where ω is the angular frequency, $A(\omega)$ is the complex amplitude, and $k(\omega)$ is the wavenumber of waves having ω , Ω is the maximum angular frequency of surface waves. The $F_{\eta}(\omega)$ is the Fourier transformation of $\eta(x, t)$ when the measurement time t_m and Ω are sufficiently large. Using the inverse Fourier transformation of $F_{\eta}(\omega)$, $\eta(x, t)$ is shown as:

$$\eta(x, t) = \frac{1}{2\pi} \int_{-\Omega}^{\Omega} F_{\eta}(\omega) e^{i\omega t} d\omega. \quad (\text{A2})$$

Comparing Eq. (A1) and (A2), $F_{\eta}(\omega)$ is $F_{\eta}(\omega) = 2\pi A(\omega) e^{-ik(\omega)x}$. Assuming that the wind waves change the shape little between two wave probes set upstream and downstream, we set the upstream and downstream water-level fluctuations to $\eta_1(\hat{t}) = \eta(0, \hat{t})$ and $\eta_2(\hat{t}) = \eta(\Delta x, \hat{t})$, respectively, with Δx downstream from the first probe. The Fourier transformations $F_{\eta_1}(\omega)$ and $F_{\eta_2}(\omega)$ for $\eta_1(t)$ and $\eta_2(t)$, respectively, are shown as:

$$F_{\eta_1}(\omega) = 2\pi A(\omega), \quad (\text{A3})$$

$$F_{\eta_2}(\omega) = 2\pi A(\omega) e^{-ik(\omega)\Delta x}. \quad (\text{A4})$$

Then, the power spectra $S_{\eta_1\eta_1}(\omega)$ and $S_{\eta_2\eta_2}(\omega)$ for $\eta_1(\hat{t})$ and $\eta_2(\hat{t})$, respectively, are shown as:

$$S_{\eta_1\eta_1}(\omega) = \frac{1}{t_m} F_{\eta_1}^*(\omega) F_{\eta_1}(\omega) = \frac{1}{t_m} 4\pi^2 |A(\omega)|^2, \quad (\text{A5})$$

$$S_{\eta_2\eta_2}(\omega) = \frac{1}{t_m} F_{\eta_2}^*(\omega) F_{\eta_2}(\omega) = S_{\eta_1\eta_1}(\omega). \quad (\text{A6})$$

Here, the superscript * indicates the complex conjugate number. The cross-spectrum $Cr(\omega)$ for $\eta_1(t)$ and $\eta_2(t)$ is shown as:

$$Cr(\omega) = \frac{1}{t_m} F_{\eta_1}^*(\omega) F_{\eta_2}(\omega) = \frac{1}{t_m} 4\pi^2 |A(\omega)|^2 e^{ik(\omega)\Delta x}. \quad (\text{A7})$$

Using Euler's theorem, Eq. (A7) transforms to:

$$\begin{aligned} Cr(\omega) &= \frac{1}{t_m} 4\pi^2 |A(\omega)|^2 (\cos k(\omega)\Delta x + i \sin k(\omega)\Delta x) \\ &= S_{\eta_1}(\omega) (\cos k(\omega)\Delta x + i \sin k(\omega)\Delta x). \end{aligned} \quad (\text{A8})$$

We can define the cospectrum $Co(\omega)$ and quad spectrum $Q(\omega)$ as the real and imaginary parts of $Cr(\omega)$, respectively, shown as:

$$Cr(\omega) = Co(\omega) + iQ(\omega) \quad (\text{A9})$$

Moreover, the phase $\theta(\omega)$ is defined as:

$$\theta(\omega) = \tan^{-1} \left(\frac{Q(\omega)}{Co(\omega)} \right), \quad (\text{A10})$$

thus,

$$\theta(\omega) = \tan^{-1} (\tan(k(\omega)\Delta x)) = k(\omega)\Delta x. \quad (\text{A11})$$

Generally, the velocity of the wind waves C is defined as:

$$C = \frac{\omega}{k} = \frac{L}{T}, \quad (\text{A12})$$

where L is the wavelength and T is the wave period. From Eqs. (A11) and (A12), $C(\omega)$ and $L(\omega)$ can be transformed to:

$$C(\omega) = \frac{\omega}{k} = \frac{\omega \Delta x}{\theta(\omega)}, \quad (\text{A13})$$

$$L(\omega) = \frac{2\pi}{k} = \frac{2\pi \Delta x}{\theta(\omega)}. \quad (\text{A14})$$

When we estimate $\theta_m(\omega_m)$ at the significant angular frequency of wind waves $\omega_m (=2\pi f_m)$, the phase velocity of the significant wind waves $C_S(\omega_m)$ and significant wavelength $L_S(\omega_m)$ are calculated by:

$$C_S = \frac{2\pi f_m \Delta x}{\theta(f_m)}, \quad (\text{A15})$$

$$L_S = \frac{2\pi \Delta x}{\theta(f_m)}. \quad (\text{A16})$$

Change in Manuscript: We revised the sentences in line 119, lines 138-142, lines 156-157, and lines 462-507 (appendix) in the mark-up manuscript.

8. Line 133: What is an “open tank”? Please explain in the manuscript.

Previous Author’s Reply: The typhoon simulation tank in IAP RAS is constructed with a large tank and a submerged wind-wave flume. The operating cross section of the airflow is 0.40 x 0.40 m², and the sidewalls are submerged at a depth of 0.30 m (see Troitskaya et al., 2012). We removed the term “open tank” in the revised manuscript and changed the sentence to “This is because the wind-wave flume at IAP RAS is a submerged flume; thus, the Stokes drift on the wavy water surface does not provide the counterflow for the bulk water, unlike in the closed tank at Kyoto University” in the revised manuscript.

Change in Manuscript: We revised the sentences in lines 171-175, lines 414-416 in the mark-up manuscript.

References

1. Donelan, M.A., Haus, B.K., Reul, N., Plant, W.J., Stiassnie, M., Graber, H.C., Brown, O.B., Saltzman, E.S., (2004), On the limiting aerodynamic roughness of the ocean in very strong winds, *Geophysical Research Letters*, 31, doi:10.1029/2004GL019460. L18306
2. Holthuijsen, L. H., M. D. Powell, and J. D. Pietrzak (2012), Wind and waves in extreme hurricanes, *J. Geophys. Res.*, 117, C09003, doi:10.1029/2012JC007983.
3. Iwano, K., Takagaki, N., Kurose, R., Komori, S., (2013), Mass transfer velocity across the breaking air-water interface at extremely high wind speeds, *Tellus B* 65, 21341, doi:10.3402/tellusb.v65i0.21341
4. Komori, S., Iwano, K., Takagaki, N., Onishi, R., Kurose, R., Takahashi, K., Suzuki, N., (2018), Laboratory measurements of heat transfer and drag coefficients at extremely high wind speeds, *Journal of Physical Oceanography*, doi:10.1175/JPO-D-17-0243.1
5. Takagaki, N., Komori, S., Suzuki, N., Iwano, K., Kuramoto, T., Shimada, S., Kurose, R., Takahashi, K., (2012), Strong correlation between the drag coefficient and the shape of the wind sea spectrum over a broad range of wind speeds, *Geophysical Research Letters*, 39, doi:10.1029/2012GL053988. L23604
6. Takagaki, N., Komori, S., Suzuki, N., Iwano, K., Kurose, R., (2016), Mechanism of drag coefficient saturation at strong wind speeds, *Geophysical Research Letters*, 43, doi:10.1002/2016GL070666
7. Troitskaya, Y. I., Sergeev, D. A., Kandaurov, A. A., Baidakov, G. A., Vdovin, M. A., Kazakov, V. I., (2012), Laboratory and theoretical modeling of air-sea momentum transfer under severe wind conditions, *Journal of Geophysical Research*, 117, C00J21, doi:10.1029/2011JC007778
8. Troitskaya, Y., A. Kandaurov, O. Ermakova, D. Kozlov, D. Sergeev & S. Zilitinkevich, (2017), Bag-breakup fragmentation as the dominant mechanism of sea-spray production in high winds, *Scientific Reports*, 7, 1614.
9. Troitskaya, Y., A. Kandaurov, O. Ermakova, D. Kozlov, D. Sergeev, S. Zilitinkevich, (2018a), The “Bag Breakup” Spume Droplet Generation Mechanism at High Winds. Part I: Spray Generation Function, 48 (9), 2167-2188.
10. Troitskaya, Y., O. Druzhinin, D. Kozlov, S. Zilitinkevich, (2018b), The “Bag Breakup” spume droplet generation mechanism at high winds. Part II: Contribution to momentum and enthalpy transfer, 48 (9), 2189-2207.

Reviewer #2:

Reply: We would like to thank reviewer #2 for reading our manuscript carefully and giving us the favorable reply. We revised the manuscript according to all reviewers. Please find the mark-up manuscript.

Effects of current on wind waves in strong winds

*Naohisa Takagaki¹, Naoya Suzuki², Yuliya Troitskaya³, Chiaki Tanaka²,
Alexander Kandaurov³, Maxim Vdovin³*

¹ (Corresponding Author) Department of Mechanical Engineering, University of Hyogo,
Shosha 2167, Himeji Hyogo, 671-2280 Japan, *E-mail: takagaki@eng.u-hyogo.ac.jp*
Tel/Fax: +81-79-267-47834

² Faculty of Science and Engineering, Kindai University, 3-4-1, Kowakae Higashiosaka
Osaka, 577-8502 Japan.

³ Department of Geophysical Research, Institute of Applied Physics, the
Russian Academy of Sciences, 46 Ul'yanov Street, Nizhny Novgorod, 603-950,
Russia.

Keywords: wind waves, current, Doppler shift

Abstract

It is important to investigate the effects of current on wind waves, called the Doppler shift, both at normal and extreme high wind speeds. Three different types of wind-wave tanks along with a fan and pump are used to demonstrate wind waves and currents in laboratories at Kyoto University, Japan, Kindai University, Japan, and the Institute of Applied Physics, Russian Academy of Sciences, Russia. Profiles of the wind and current velocities and the water-level fluctuation are measured. The wave frequency, wavelength, and phase velocity of the significant waves are calculated, and the water velocities at the water surface and in the bulk of the water are also estimated by the current distribution. The study investigated 27 cases with carrying winds, waves, and currents, at wind speeds ranging from 7 to 67 m s⁻¹. The results show that 27 different types of currents can be generated at wind speeds ranging from 7 to 67 m s⁻¹. At normal wind speeds under 30 m s⁻¹, wave frequency, wavelength, and phase velocity depend on wind speed and fetch. The effect of the Doppler shift is confirmed at normal wind speeds, i.e., the significant waves are accelerated by the surface current. The phase velocity can be represented as the sum of the surface current and artificial phase velocity, which is estimated by the dispersion relation of the deep-water waves. At extreme high wind speeds, over 30 m s⁻¹, a similar Doppler shift is observed as under the conditions of normal wind speeds. This suggests

35 that the Doppler shift is an adequate model for representing the acceleration of wind
36 waves by current, not only for the wind waves at normal wind speeds but also for those
37 with intensive breaking at extreme high wind speeds. A weakly nonlinear model of
38 surface waves at a shear flow is developed. It is shown that it describes well the
39 dispersion properties of not only small-amplitude waves but also strongly nonlinear and
40 even breaking waves, typical for extreme wind conditions (over 30 m s^{-1}).

41

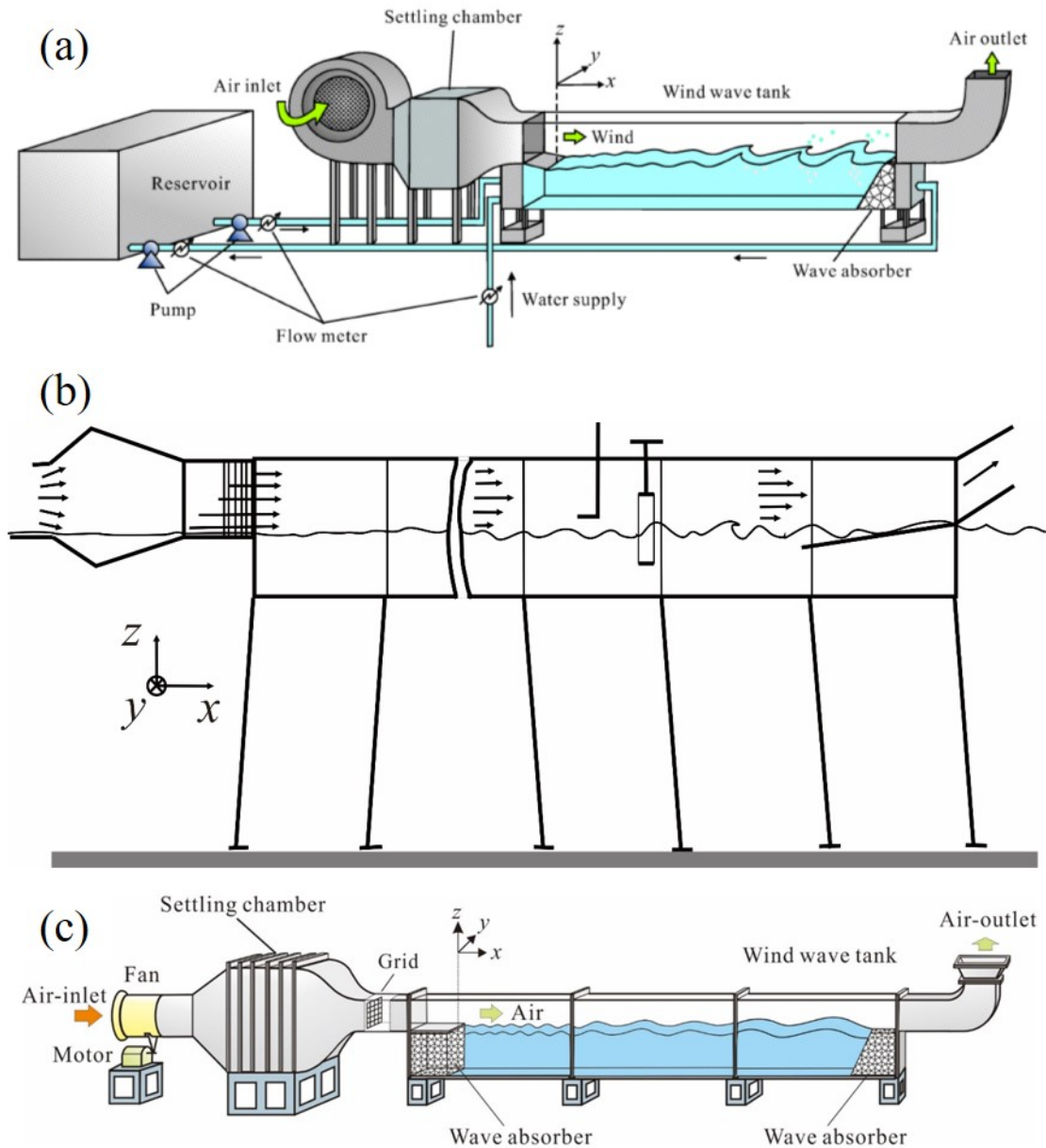
42 **1. Introduction**

43 The oceans flow constantly, depending on the rotation of the Earth ~~earth's rotation~~,
44 tides, ~~ground-shape~~ topography, and wind shear. High-speed continuous ocean flows are
45 called currents. Although the mean surface velocity of the ocean is approximately 0.1 m
46 s^{-1} , ~~the maximum surface velocity for the currents is 1 m/s~~ the maximum current surface
47 velocity is more than 1 m s^{-1} (e.g., Kawabe, 1988; Kelly et al., 2001). The interaction
48 between the current and wind waves generated by ~~the~~ wind shear have been investigated
49 in several studies. The acceleration effects of the current on wind waves, called the
50 Doppler shift; (well-known as the Doppler shift), the effects of the current on the
51 momentum and heat transfer across the sea surface; a sea surface, and the modeling of
52 waves and currents in the Gulf Stream have been the subject of experimental and
53 numerical investigations (e.g., Dawe and Thompson, 2006; Kara et al., 2007; Fan et al.,
54 2009; Shi and Bourassa, 2019). Thus, wind waves follow the dispersion relationship and
55 Doppler shift effect at normal wind speeds. However, these studies were performed at
56 normal wind speeds only, and few studies have been conducted at extreme high wind
57 speeds, for which the threshold velocity is $30 - 35 \text{ m s}^{-1}$, representing the regime shift of
58 the air-sea momentum, heat, and mass transport (Powell et al., 2003; Donelan et al., 2004;
59 Takagaki et al., 2012, 2016; Troitskaya et al., 2012, 2020; Iwano et al., 2013; Krall and
60 Jähne, 2014; Komori et al., 2018; Krall et al., 2019). At such extremely high wind speeds,
61 the water surface is intensively broken by the strong wind shear, along with the foam
62 layer, dispersed droplets, and entrained bubbles (e.g. Donelan et al., 2004; Troitskaya et
63 al., 2012, 2017, 2018a, 2018b; Takagaki et al., 2012, 2016; Holthuijsen et al., 2012). It is
64 unclear if the properties of wind waves and the surface foam layer at extremely high wind
65 speeds are similar to those at normal wind speeds. Furthermore, in a hurricane, the local
66 ocean flows may be unusually strong, change rapidly, and strongly affect wind waves. At
67 ~~such extreme high wind speeds, owing to the intensive breaking by the strong wind shear,~~
68 ~~the local ocean flows might be strong.~~ Furthermore, under a hurricane, the directions of
69 ~~the wind and ocean flows rapidly change; thus, the wind waves under a hurricane might~~

70 ~~be strongly affected by complicated local ocean flows.~~ However, the effects of the current
71 on wind waves have not yet been clarified.

72 Therefore, the purpose of this study is to investigate the effects of the current on wind
73 waves in strong winds through the application of three different types of wind-wave tanks,
74 along with a pump.

75



76

77 **Figure 1.** Schematics of wind-wave tanks. (a) High-speed wind-wave tank of Kyoto University. (b)

78

79 Typhoon simulator of IAP RAS. (c) Wind-wave tank of Kindai University.

79

80

81

82 2. Experiment

83 2.1. Equipment and measurement methods

84 Wind-wave tanks at Kyoto University, Japan and the Institute of Applied Physics,
85 Russian Academy of Sciences (IAP RAS) were used in the experiments (Figs. 1a, 1b).
86 For the tank at Kyoto University, the glass test section was 15 m long, 0.8 m wide, and 1.6
87 m high. The water depth D was set at 0.8 m. For the tank at IAP RAS, the test section in
88 the air side was 15 m long, 0.4 m wide, and 0.4 m high. The water depth D was set at 1.5
89 m. The wind was set to blow over the filtered tap water in these tanks, generating wind
90 waves. The wind speeds ranged from 4.7 to 43 m s⁻¹ and from 8.5 to 21 m s⁻¹ in the tanks
91 at Kyoto and IAP RAS, respectively. Measurements of the wind speeds, water-level
92 fluctuation, and current were carried out 6.5 m downstream from the edge ($x = 0$ m) in
93 both the Kyoto and IAP RAS tanks. Here, the x , y , and z coordinates are referred to as the
94 streamwise, spanwise, and vertical directions, respectively, with the origin located at the
95 center of the edge of the entrance plate. Additionally, the fetch (x) is defined as the
96 distance between the origin and measurement point ($x = 6.5$ m).

97 In Kyoto, a laser Doppler anemometer (Dantec Dynamics LDA) and phase Doppler
98 anemometer (Dantec Dynamics PDA) were used to measure the wind velocity fluctuation.
99 A high-power multi-line argon-ion (Ar⁺) laser (Lexel model 95-7; laser wavelengths of
100 488.0 and 514.5 nm) with a power of 3 W was used. The Ar⁺ laser beam was shot through
101 the sidewall (glass) of the tank. Scattered particles with a diameter of approximately 1 μm
102 were produced by a fog generator (Dantec Dynamics F2010 Plus) and were fed into the
103 air flow over the waves (see Takagaki et al. (2012) and Komori et al. (2018) for details).
104 The wind speed values (U_{10}) at a height of 10 m height above the ocean and the friction
105 velocity (u^*) were estimated by the eddy correlation method, by which the mean velocity
106 (U) and the Reynolds stress ($-uv$) in air were measured. The u^* was estimated by an eddy
107 correlation method as $u^* = (-\langle uv \rangle)^{1/2}$, because the shear stress at the interface (τ) was
108 defined by $\tau = \rho u^{*2} = \rho C_D U_{10}^2$. The value of $(-\langle uv \rangle)^{1/2}$ was estimated by extrapolating the
109 measured values of the Reynolds stress to the mean surface of $z = 0$ m. The U_{10} was
110 estimated by the log-law: $U_{10} - U_{\min} = u^*/\kappa \ln(z_{10}/z_{\min})$, where U_{\min} is the air velocity
111 nearest the water surface (z_{\min}) and z_{10} is 10 m. Moreover, the drag coefficient C_D was
112 estimated by $C_D = (u^*/U_{10})^2$.

113 Water level fluctuations were measured using resistance-type wave gauges (Kenek
114 CHT4-HR60BNC) in Kyoto. The resistance wire was placed into the water, and the
115 electrical resistance at the instantaneous water level was recorded at 500 Hz for 600 s
116 using a digital recorder (Sony EX-UT10). The energy of the wind waves (E) was

117 estimated by integrating the spectrum of the water-level fluctuations over the frequency
 118 (f). The values of the wavelength (L_S) and phase velocity (C_S) were estimated using the
 119 ~~eospectra~~ cross-spectrum method (e.g., Takagaki et al., 2017) (see the detail in Appendix).
 120 The current was measured using the same LDA system.

121 In IAP RAS, a hot-wire anemometer (E+E Elektrik EE75) was used to measure the
 122 representative mean wind velocity at $x = 0.5$ m and $z = 0.2$ m. The three wind velocities
 123 (U_{10} , u^* , U_∞) at $x = 6.5$ m were taken from Troitskaya et al. (2012) by a Pitot tube. Here,
 124 U_∞ is the freestream wind speed. The u^* was estimated by a profile method considering
 125 the profiles in the constant flux layer and the wake region:

$$126 \quad U_\infty - U(z) = u^* \left(-\frac{1}{\kappa} \ln(z/\delta) + \alpha \right); z/\delta < 0.15, \quad (1)$$

$$127 \quad U_\infty - U(z) = \beta u^* (1 - z/\delta)^2; z/\delta > 0.15, \quad (2)$$

128 respectively. Here, δ is the boundary layer thickness, and α and β are the constant values
 129 that depend on flow fields and are calibrated at low wind speeds without the dispersed
 130 droplets. At extremely high wind speeds, measuring the profile in the constant flux layer
 131 (Eq. 1) is difficult because of the large waves; thus, using β measured at low wind speeds,
 132 u^* is estimated by Eq. (2). The value of U_{10} is estimated by Eq. (1) at $z_{10} = 10$ m with
 133 measured α at normal wind speeds. The value of C_D is estimated by $C_D = (u^*/U_{10})^2$.
 134 Although the measurement methods for u^* , U_{10} , and C_D in IAP RAS and Kyoto are
 135 different, the values approximately correspond to each other (see Troitskaya et al. (2012)
 136 and Takagaki et al. (2012)).

137 The water-level fluctuations were measured using three handmade capacitive-type
 138 wave gauges in IAP RAS. Three wires formed a triangle with 25 mm on a side
 139 (x-directional distance between wires Δx is 21.7 mm). The wires were placed in the water,
 140 and the output voltages at the instantaneous water level were recorded at 200 Hz for 5400
 141 s using a digital recorder through an AD converter (L-Card E14-140). The values (E , f_m ,
 142 H_S , T_S , C_S , and L_S) were estimated by the same mannar as in Kyoto tank. The current was
 143 measured through acoustic Doppler velocimetry (Nortec AS) at $x = 6.5$ m and $z = -10$,
 144 -30 , -50 , -100 , -150 , -220 , and -380 mm (see Troitskaya et al. (2012) for details).

145

146 **2.2. Artificial current experiments at Kindai University**

147 Additional experiments were performed using a wind-wave tank at Kindai
 148 University with a glass test section 6.5 m long, 0.3 m wide, and 0.8 m high (Fig. 1c) (e.g.
 149 Takagaki et al., 2020). The water depth D was set at 0.49 m. A Pitot tube (Okano Works,

150 LK-0) and differential manometers (Delta Ohm HD402T) were used to measure the mean
151 wind velocity. The values of u^* , U_{10} , and C_D (Cases 21-27) were estimated using U_∞ by
152 the empirical curve by Iwano et al. (2013), which was proposed by the eddy correlation
153 method used in Kyoto (see section 2.1).

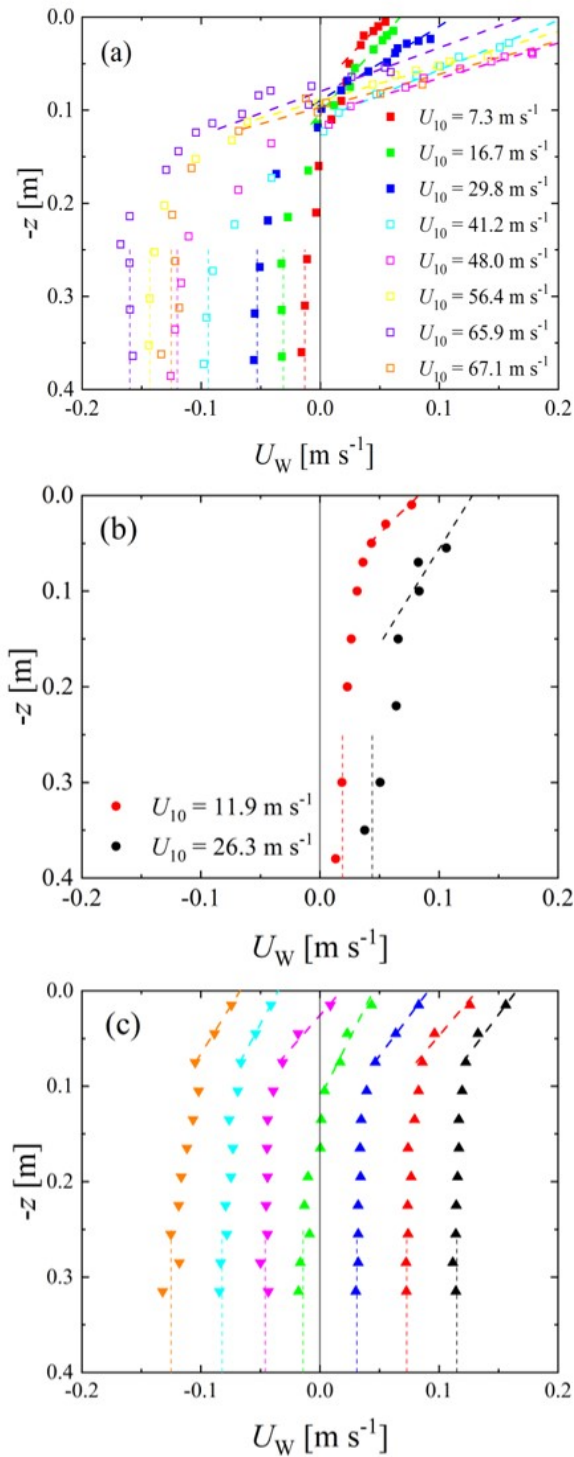
154 The water level fluctuations were measured using resistance-type wave gauges
155 (Kenek CHT4-HR60BNC). To measure L_S and C_S , another wave gauge was fixed
156 downstream at $\Delta x = 0.02$ m, where Δx is the interval between the two wave gauges. The
157 values (E , f_m , H_S , T_S , C_S , and L_S) were estimated by the same manner as in Kyoto tank.
158 The current was then measured through electromagnetic velocimetry (Kenek LP3100)
159 with a probe (Kenek LPT-200-09PS) at $x = 4.0$ m. The probe sensing station was 22 mm
160 long with a diameter of 9 mm. The measurements were performed at $z = -15$ to -315 mm
161 at 30 mm intervals. The sampling frequency was 8 Hz, and the sampling time was 180 s.

162

163 **3. Results and discussion**

164 **3.1. Waves and current**

165 Figure 2 shows the vertical distributions of the streamwise water velocity. The
166 water velocities in the three different wind-wave tanks at Kyoto University, Kindai
167 University, and IAP RAS are separately shown in each subfigure. In Fig. 2a, the bulk
168 velocity of water U_{BULK} shows negative values ($U_{\text{BULK}} = -0.16$ to -0.01 m s⁻¹) at Kyoto
169 University, which is generated as the counterflow against the Stokes drift at the wavy
170 water surface. In Fig. 2b, the bulk velocity of water demonstrates positive values (U_{BULK}
171 $= 0.019$ to 0.044 m/s) at IAP RAS, because the wind-wave flume is submerged; thus, the
172 Stokes drift on the wavy water surface does not provide the counterflow for the bulk
173 water, unlike in the closed tank at Kyoto University. This is because the wind-wave tank
174 at IAP RAS is an open tank; thus, the Stokes drift on the wavy water surface does not
175 provide the counterflow for the bulk water, unlike in the closed tank at Kyoto University.
176 From Fig. 2c, it is clear that the bulk velocities of the water vary in each case at Kindai
177 University with the use of the pump. Furthermore, the water bulk velocities change from
178 negative to positive ($U_{\text{BULK}} = -0.13$ to -0.17 m s⁻¹). The bulk velocities of water were
179 defined as the mean velocity with $z = -0.4$ to -0.25 m (see dotted lines in Fig. 2), and the
180 velocities are listed in Table 1. Experiments were performed under 27 different conditions,
181 with the bulk velocity of water provided in the three different wind-wave tanks. The
182 surface velocities of water, U_{SURF} , also varied in the three tanks with respect to wind
183 speed (see Fig. 2). The U_{SURF} values were estimated by the linear extrapolation lines
184 (dashed lines) as the water velocity at the surface ($z = 0$ m) shown in Fig. 2, and the
185 velocities are listed in Table 1.



186

187 **Figure 2.** Vertical distributions of water-flow velocity; (a) Kyoto University, (b) IAP RAS, and (c)

188 Kindai University. In (c), plots indicate cases 21–27 starting from right. Dotted and dashed lines

189 indicate the lines used to estimate U_{BULK} and U_{SURF} , respectively. Open symbols show the

190 high-wind-speed cases.

191 **TABLE 1.** Wind and wind-wave properties. F : fetch; N_{PUMP} : pump inverter frequency; U_{∞} :
 192 freestream wind speed; u^* : friction velocity of air; U_{10} : wind speed at 10 m above the sea surface;
 193 U_{SURF} : surface flow velocity of water; U_{BULK} : bulk flow velocity of water; C_D : drag coefficient; H_s :
 194 significant wave height; T_s : significant wave period; E : wave energy; f_m : significant frequency; C_s :
 195 phase velocity; L_s : significant wave length; $C_{s\text{-theor-l}}$: phase velocity predicted by theoretical linear
 196 model; $C_{s\text{-theor-nl}}$: phase velocity predicted by theoretical nonlinear model. The values of u^* , U_{10} , and
 197 C_D in Kindai were estimated using the empirical curves by Iwano et al. (2013) from U_{∞} . Superscripts †
 198 and †† indicate the artificial following and opposing flows, respectively.

Case	Facility	F	N_{pump}	U_{∞}	u^*	U_{10}	U_{SURF}	U_{BULK}	C_D	H_s	T_s	$E^{0.5}$	f_m	C_s	L_s	$C_{s\text{-theor-l}}$	$C_{s\text{-theor-nl}}$
		[m]	[Hz]	[m s ⁻¹]	[m s ⁻¹]	[m s ⁻¹]	[m s ⁻¹]	[m s ⁻¹]	[$\times 10^{-3}$]	[m]	[m]	[m]	[Hz]	[m s ⁻¹]	[m]	[m s ⁻¹]	[m s ⁻¹]
1	Kyoto	6.5	-	4.7	0.24	7.3	0.056	-0.01	1.1	0.0035	0.15	0.00092	6.63	0.40	0.06	0.369	0.374
2	Kyoto	6.5	-	7.2	0.43	11.5	-	-	1.4	0.0131	0.25	0.00353	3.95	0.59	0.16	-	-
3	Kyoto	6.5	-	10.3	0.67	16.7	0.067	-0.031	1.6	0.0231	0.32	0.00624	3.03	0.69	0.23	0.658	0.690
4	Kyoto	6.5	-	12.6	0.89	21.5	-	-	1.7	0.0357	0.39	0.00968	2.59	0.92	0.38	-	-
5	Kyoto	6.5	-	16.3	1.49	29.8	0.112	-0.053	2.5	0.0584	0.50	0.01570	2.01	1.09	0.52	0.972	1.044
6	Kyoto	6.5	-	18.8	1.70	33.6	-	-	2.5	0.0626	0.52	0.01691	1.89	1.18	0.60	-	-
7	Kyoto	6.5	-	22.2	2.08	41.2	0.206	-0.094	2.6	0.0631	0.53	0.01735	1.86	1.35	0.74	1.188	1.258
8	Kyoto	6.5	-	24.8	-	-	-	-	-	0.0668	0.55	0.01866	1.76	1.41	0.79	-	-
9	Kyoto	6.5	-	28.5	2.36	48.0	0.273	-0.120	2.4	0.0727	0.58	0.02058	1.68	1.54	0.93	1.325	1.424
10	Kyoto	6.5	-	31.1	-	-	-	-	-	0.0807	0.62	0.02309	1.58	1.60	1.07	-	-
11	Kyoto	6.5	-	34.8	2.69	56.4	0.241	-0.143	2.3	0.0944	0.68	0.02715	1.44	1.64	1.10	1.379	1.550
12	Kyoto	6.5	-	37.1	2.89	57.7	-	-	2.5	0.1043	0.73	0.03027	1.37	1.76	1.31	-	-
13	Kyoto	6.5	-	39.6	3.38	65.9	0.170	-0.160	2.6	0.1214	0.80	0.03553	1.20	1.84	1.51	1.531	1.694
14	Kyoto	6.5	-	43.3	3.31	67.1	0.272	-0.125	2.4	0.1609	0.93	0.04766	1.08	2.01	1.92	1.743	2.149
15	IAP RAS	6.5	-	8.5	0.40	11.9	0.083	0.019	1.1	0.0214	0.31	0.0056	3.14	0.78	0.25	0.690	0.715
16	IAP RAS	6.5	-	11.0	0.60	16.7	-	-	1.3	0.0305	0.36	0.0081	2.84	0.89	0.32	-	-
17	IAP RAS	6.5	-	13.5	0.90	21.9	-	-	1.7	0.0455	0.43	0.0121	2.41	1.07	0.45	-	-
18	IAP RAS	6.5	-	16.3	1.15	26.3	0.128	0.044	1.9	0.0790	0.50	0.0161	1.95	1.27	0.65	1.111	1.190
19	IAP RAS	6.5	-	18.9	1.50	32.5	-	-	2.1	0.0690	0.54	0.0246	1.85	1.37	0.74	-	-
20	IAP RAS	6.5	-	21.2	1.70	36.9	-	-	2.1	0.0847	0.60	0.0305	1.61	1.61	1.00	-	-
21	Kindai	4.0	15 [†]	5.8	0.28	7.9	0.165	0.115	1.2	0.0044	0.14	0.0012	6.92	0.43	0.06	0.484	0.492
22	Kindai	4.0	10 [†]	5.8	0.28	7.9	0.132	0.073	1.2	0.0050	0.16	0.0014	6.10	0.43	0.07	0.501	0.510
23	Kindai	4.0	5 [†]	5.8	0.28	7.9	0.091	0.031	1.2	0.0049	0.16	0.0014	6.16	0.38	0.06	0.410	0.420
24	Kindai	4.0	0	5.8	0.28	7.9	0.045	-0.014	1.2	0.0054	0.19	0.0014	5.47	0.38	0.07	0.382	0.393
25	Kindai	4.0	5 ^{††}	5.8	0.28	7.9	0.018	-0.046	1.2	0.0076	0.23	0.0021	4.25	0.36	0.08	0.384	0.400
26	Kindai	4.0	10 ^{††}	5.8	0.28	7.9	-0.035	-0.082	1.2	0.0098	0.27	0.0027	3.64	0.35	0.10	0.355	0.375
27	Kindai	4.0	15 ^{††}	5.8	0.28	7.9	-0.067	-0.125	1.2	0.0125	0.34	0.0035	2.94	0.38	0.13	0.381	0.402

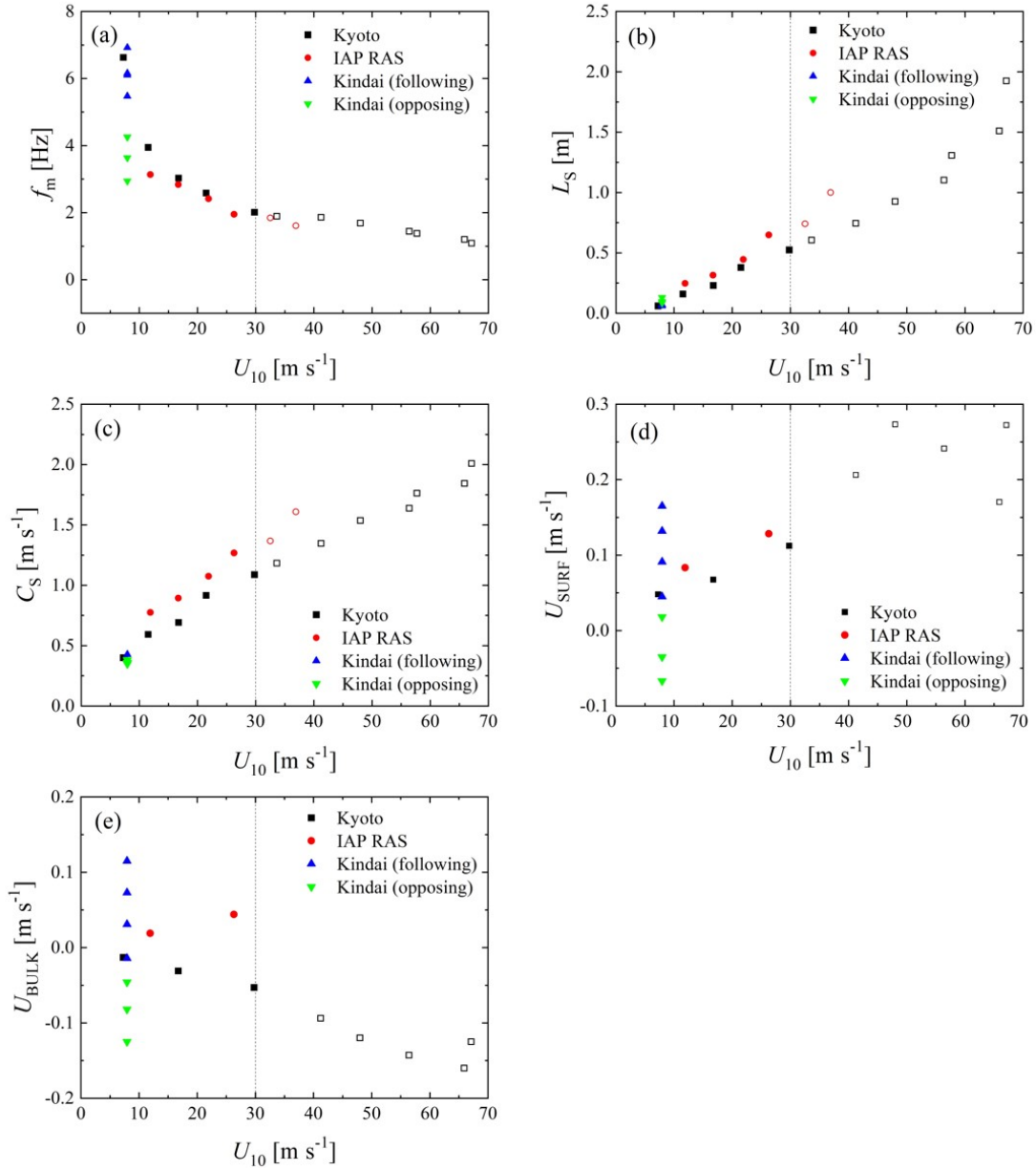
199

200

201

202 Figure 3 shows the wind-velocity dependency of the wave frequency f_m ,
 203 wavelength L_s , phase velocity C_s , surface velocity of water U_{SURF} , and bulk velocity of
 204 water U_{BULK} . From Figs. 3a–3c, it is clear that both the Kyoto and IAP RAS data
 205 demonstrate that the wind waves develop with wind shear. Although f_m in both cases
 206 correspond to each other, L_s and C_s in IAP RAS are different from those in Kyoto. The
 207 disagreement might be caused by the difference in the wind-wave development or
 208 Doppler effect; this is discussed below. From Figs. 3d and 3e, U_{SURF} and U_{BULK} increase

209



210

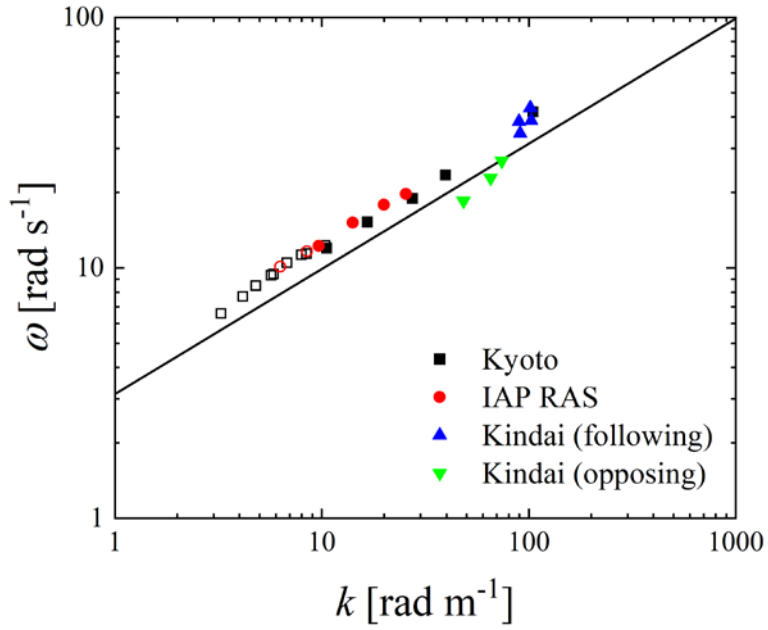
211 **Figure 3.** Relationships between U_{10} and (a) significant frequency f_m , (b) significant wave length L_s ,

212 (c) phase velocity C_s , (d) surface velocity of water U_{SURF} , and (e) bulk velocity of water U_{BULK} . Open

213

symbols show the high-wind-speed cases.

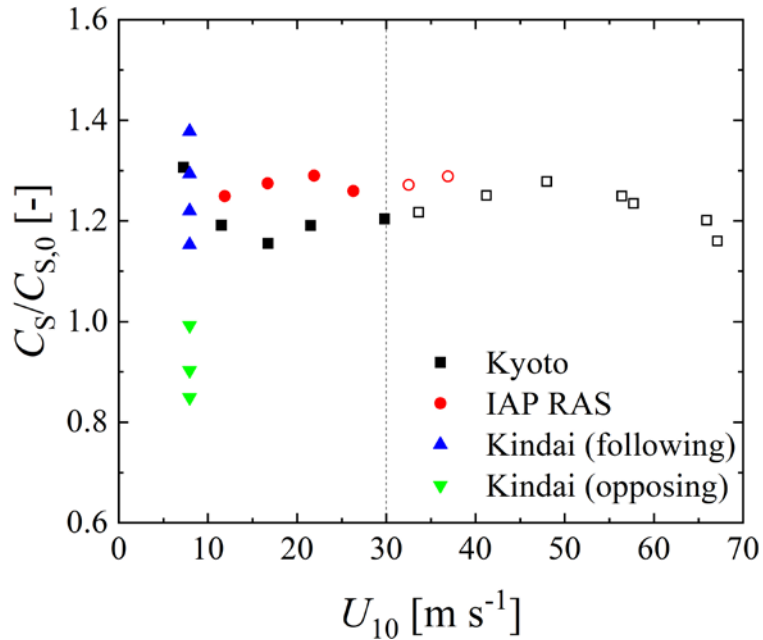
214



215

216 **Figure 4.** Dispersion relation between angular frequency ω and wave number k . Open symbols show
 217 the high-wind-speed cases. Curve shows the dispersion relation of the deep-water waves ($\omega^2 = gk$).

218



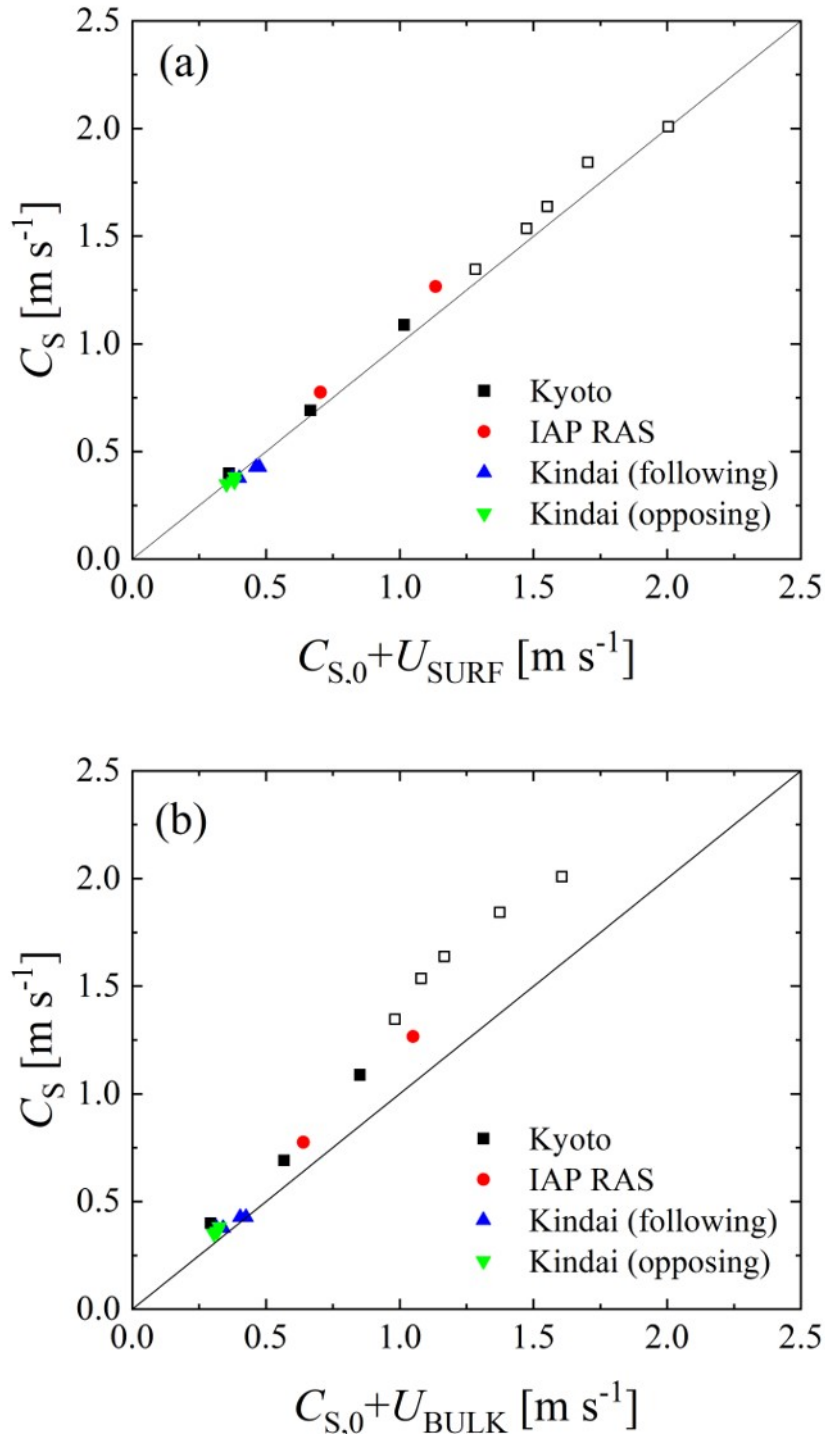
219

220 **Figure 5.** Relationship between the freestream wind speed and phase velocity C_s . The C_s is
 221 normalized by phase velocity $C_{s,0}$ without the Doppler effect, estimated by the dispersion relation of
 222 the deep-water waves ($C_{s,0} = (gL_s/2\pi)^{1/2}$). Open symbols show the high-wind-speed cases.

223 with an increase in U_{10} in IAP RAS. However, in Kyoto, U_{SURF} increases, but U_{BULK}
 224 decreases with an increase in U_{10} . Moreover, U_{SURF} in IAP RAS corresponds to U_{SURF} in
 225 Kyoto. This is because the Stokes drift generated by the wind waves, rather than the
 226 current, is significant. For the Kindai data, although f_m , U_{SURF} , and U_{BULK} vary, L_S and C_S
 227 are concentrated at single points at $L_S = 0.1$ m and $C_S = 0.4$ m s⁻¹, respectively. This shows
 228 that the intensity and direction of the current do not significantly affect L_S and C_S but do
 229 affect f_m and U_{SURF} . Thus, this implies that the present artificial current changes the water
 230 flow dramatically but does not affect the development of the wind waves.

231 Figure 4 shows the dispersion relation and demonstrates that the Kindai data
 232 points depend on the variation in the water velocity of the artificial current. The plots for
 233 the Kyoto University and IAP RAS cases at normal wind speeds (solid symbols) are
 234 concentrated above the solid curve, showing the dispersion relation of the deep-water
 235 waves ($\omega^2 = gk$). Meanwhile, the plots for extreme high wind speeds (open symbols) are
 236 also concentrated above the solid curve. This implies that the wind waves, along with the
 237 intensive breaking at extreme high wind speeds, are dependent on the Doppler shift. To
 238 investigate the phase velocity trend, Fig. 5 shows the ratio of the measured phase velocity
 239 C_S to the phase velocity $C_{S,0}$ estimated by the dispersion relation of the deep-water waves
 240 ($C_{S,0} = (gL_S/2\pi)^{1/2}$) against the wind velocity. From the figure, the ratios at the normal
 241 wind speeds assume a constant value (~ 1.21 in Kyoto or ~ 1.27 in IAP RAS). Moreover,
 242 the ratios at the extreme high wind speeds take similar values of 1.23 and 1.28 for Kyoto
 243 or IAP RAS, respectively. This implies that the phase velocities at extreme high wind
 244 speeds are accelerated by the current just as those at normal wind speeds. However, the
 245 Kindai values are scattered and increase in the following cases and decrease in the
 246 opposing cases. It is clear that the artificial current accelerates (or decelerates) the phase
 247 velocity.

248 To interpret the relationship among the measured phase velocity C_S , first phase
 249 velocity $C_{S,0}$ estimated by the dispersion relation, and water velocity, two types of phase
 250 velocity were evaluated: the sum of $C_{S,0}$ and surface velocity of water U_{SURF} and the sum
 251 of $C_{S,0}$ and bulk velocity of water U_{BULK} . Figure 6 shows the relationship between C_S and
 252 (a) $C_{S,0} + U_{\text{SURF}}$, and (b) $C_{S,0} + U_{\text{BULK}}$. In Fig. 6a, we can see that the Doppler shift is
 253 confirmed at the normal wind speeds, i.e., the significant waves are accelerated by the
 254 surface flow, and the real phase velocity can be represented as the sum of the velocity of
 255 the surface flow and the virtual phase velocity, which is estimated by the dispersion
 256 relation of the deep-water waves. At extreme high wind speeds over 30 m s⁻¹, a similar
 257 Doppler shift is observed as under the conditions of normal wind speeds, as seen in Fig.
 258 6a. Meanwhile, in Fig. 6b, although C_S corresponds to $C_{S,0} + U_{\text{BULK}}$ at low phase



259

260 **Figure 6.** Relationship between phase velocity C_S and (a) sum of $C_{S,0}$ and surface velocity of water
 261 U_{SURF} , and (b) sum of $C_{S,0}$ and bulk velocity of water U_{BULK} . Open symbols show the high-wind-speed
 262 cases.

263

264 velocities, C_S assumes values larger than $C_{S,0} + U_{\text{BULK}}$ at high phase velocities. This
 265 suggests that the Doppler shift is an adequate model for representing the acceleration of
 266 the wind waves by the current, not only for the wind waves at normal wind speeds but
 267 also for those with intensive breaking at extreme high wind speeds. Moreover, the
 268 Doppler shift of wind waves occurs due to a very thin surface flow, as the correlation
 269 between C_S and $C_{S,0} + U_{\text{SURF}}$ is higher than the correlation between C_S and $C_{S,0} + U_{\text{BULK}}$.
 270

271 **3.2. The theoretical model of waves at the shear flow**

272 The parameters of the observed Doppler shift can be explained more precisely
 273 within the theoretical model of the capillary-gravity waves at the surface of the water
 274 flows with the velocity profiles prescribed by the experimental data, which are plotted in
 275 Fig. 2a–c. Because the dominant wind wave propagates along the wave and water flows,
 276 we will consider the 2D-wave model in the 2D flow. This flow is described by the system
 277 of 2D Euler equations:

$$278 \quad \frac{\partial u}{\partial t} + u \frac{\partial u}{\partial x} + w \frac{\partial u}{\partial z} + \frac{1}{\rho} \frac{\partial p}{\partial x} = 0, \quad (3)$$

$$279 \quad \frac{\partial w}{\partial t} + u \frac{\partial w}{\partial x} + w \frac{\partial w}{\partial z} + \frac{1}{\rho} \frac{\partial p}{\partial z} = -g,$$

280 and the condition of non-compressibility:

$$281 \quad \frac{\partial u}{\partial x} + \frac{\partial w}{\partial z} = 0, \quad (4)$$

282 with the kinematical

$$283 \quad \frac{\partial \eta}{\partial t} + u \frac{\partial \eta}{\partial x} = w \Big|_{z=\eta(x,t)} \quad (5)$$

284 and dynamical boundary conditions

$$285 \quad p \Big|_{z=\eta(x,t)} = 0 \quad (6)$$

286 at the water surface. Here, u and w are the horizontal and vertical velocity components, p
 287 is the water pressure, x and z are the horizontal and upward vertical coordinates, g is the
 288 gravity acceleration, and ρ is the water density. The boundary condition at the bottom of
 289 the channel is $w \Big|_{z=-D} = 0$. It should be noted that the water depth in almost all the
 290 experimental runs exceeded half of the wavelength of the dominant waves (see Table 1).
 291 In this case, the deep-water approximation is applicable for describing the surface waves,

292 and the boundary condition of the wave field vanishing with the distance from the water
293 surface can also be used.

294 Because the fluid motion under consideration is 2D, the stream function can be
295 introduced as follows:

$$296 \quad u = \frac{\partial \psi}{\partial z}; w = -\frac{\partial \psi}{\partial x}. \quad (7)$$

297 To derive the linear dispersion relation for the surface waves at the plane shear flow with
298 the horizontal velocity profile $U_w(z)$, we consider the solution to Eqs. ~~(1,2)~~ (3,4) in terms
299 of the stream function as the sum of the undisturbed state with steady shear flow and
300 small-amplitude disturbances. Then, the stream function ψ and pressure p are as follows:

$$301 \quad \psi(x, z, t) = \int^z U_w(z_1) dz_1 + \varepsilon \psi_1(x, z, t); \quad (8)$$

$$302 \quad p(x, z, t) = -\rho g z + \varepsilon p_1(x, z, t), \quad (9)$$

303 where $\varepsilon \ll 1$, and the water elevation value is also the order of ε , namely $\varepsilon \eta_1(x, t)$.

304 In the linear approximation in ε , the system of Eqs. ~~(1,2)~~ (3,4) and the boundary
305 conditions of Eqs. ~~(3,4)~~ (5,6) take the form:

$$306 \quad \left(\frac{\partial}{\partial t} + \frac{U_w(z) \partial}{\partial x} \right) \left(\frac{\partial^2 \psi_1}{\partial x^2} + \frac{\partial^2 \psi_1}{\partial z^2} \right) - \frac{\partial \psi_1}{\partial x} \frac{d^2 U_w(z)}{dz^2} = 0,$$

$$307 \quad \frac{\partial \eta_1}{\partial t} + U_w(0) \frac{\partial \eta_1}{\partial x} = - \frac{\partial \psi_1}{\partial x} \Big|_{z=0}, \quad (10)$$

$$308 \quad \frac{\partial p_1}{\partial x} \Big|_{z=0} - \rho g \frac{\partial \eta_1}{\partial x} = 0,$$

$$309 \quad \psi_1 \Big|_{z=-D} = 0.$$

310 Excluding p_1 with use of the first equation of the system in Eq. ~~(4)~~ (3) and eliminating η_1
311 yields one boundary condition at the water surface for ψ_1 :

$$312 \quad \left[\left(\frac{\partial}{\partial t} + \frac{U_w(0) \partial}{\partial x} \right)^2 \frac{\partial \psi_1}{\partial z} - \left(\frac{\partial}{\partial t} + U_w(0) \frac{\partial}{\partial x} \right) \frac{\partial \psi_1}{\partial x} \frac{dU_w}{dz} - g \frac{\partial^2 \psi_1}{\partial x^2} \right] \Big|_{z=0} = 0. \quad (11)$$

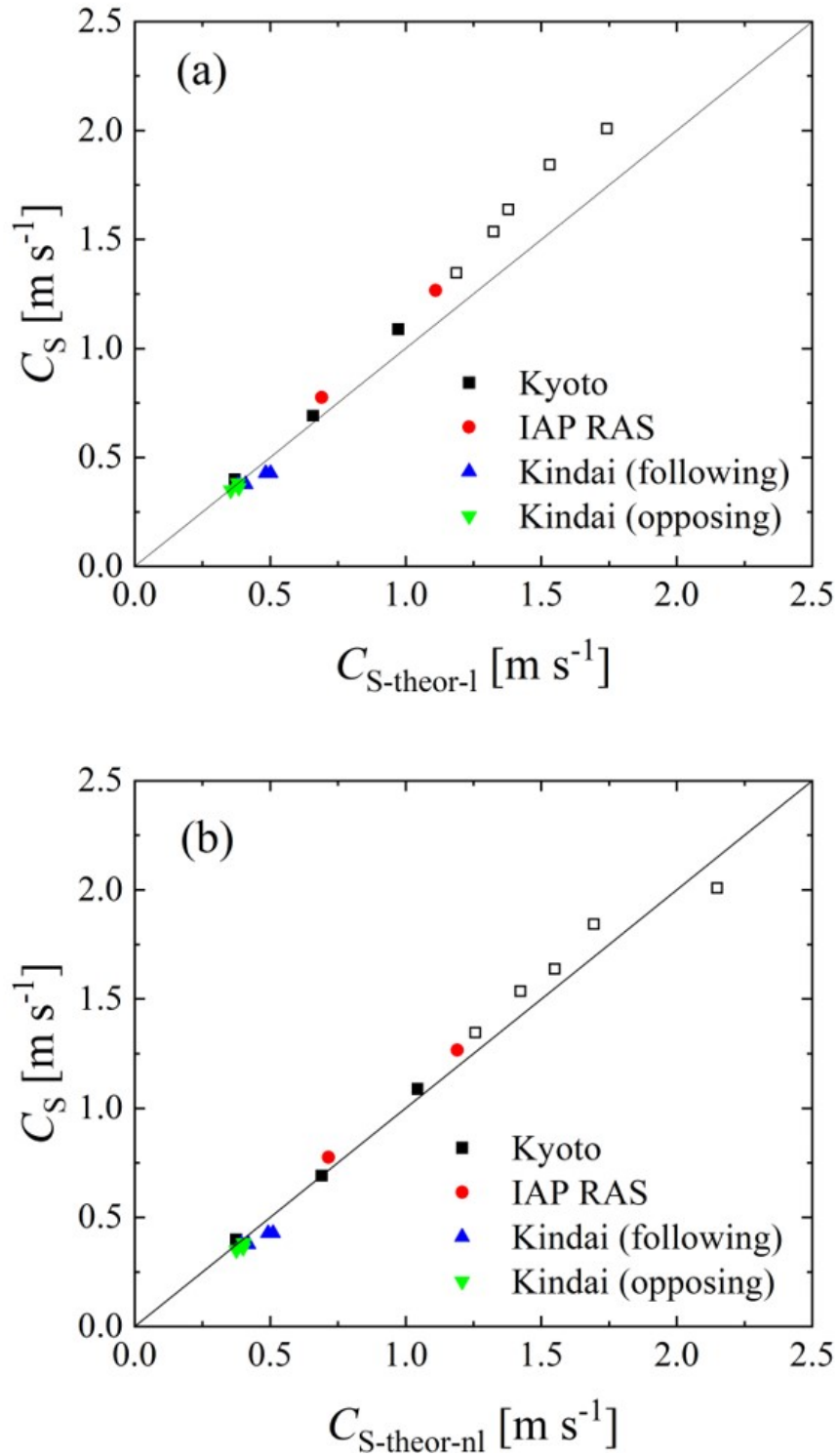
313 For the harmonic wave disturbance, where

$$314 \quad \psi_1(x, z, t) = \Psi(t) \exp(-i(\omega t - kt)), \quad (12)$$

315 substituting into Eqs. ~~(8,9)~~ (10,11) yields the Rayleigh equation for the complex
316 amplitude of the stream function disturbance:

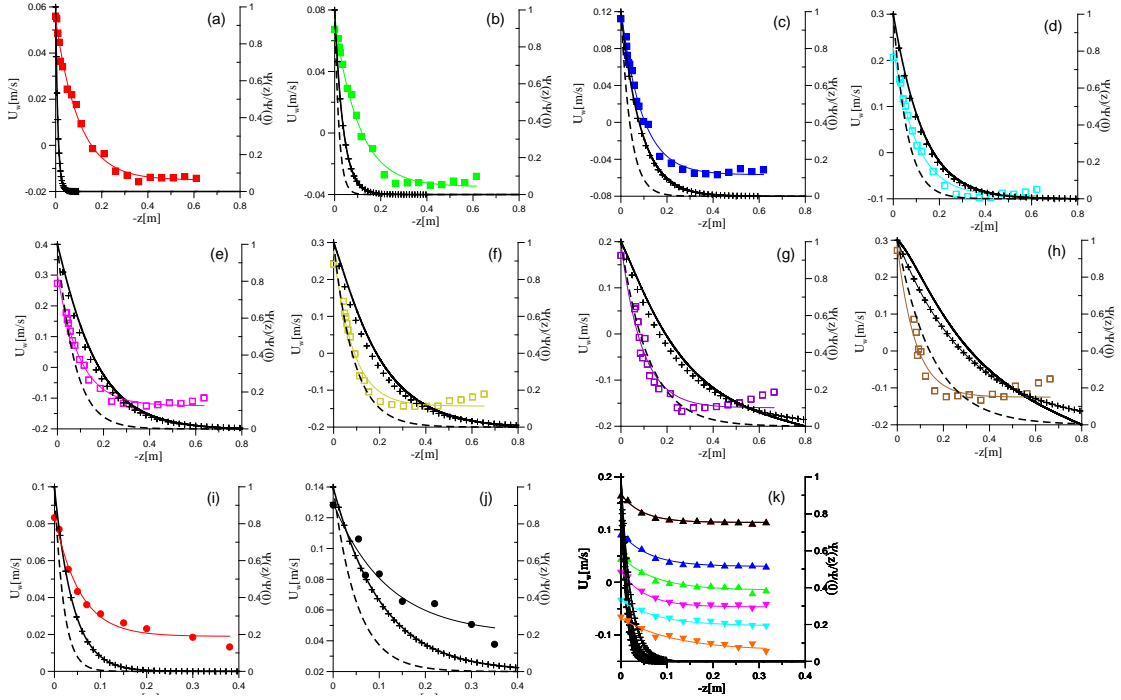
$$317 \quad (\omega - U_w(z)k) \left(\frac{d^2 \Psi_1}{dz^2} - k^2 \Psi_1 \right) + \frac{d^2 U_w(z)}{dz^2} k^2 \Psi_1 = 0, \quad (13)$$

318 with the following boundary condition:



319
320
321
322

Figure 7. The measured phase velocity C_S versus theoretical prediction: (a) linear model, and (b) nonlinear model.



323

324 **Figure 8.** Vertical velocity profiles (points), their fitting (thin color line), the eigenfunction of the Eq.
 325 (8) with the boundary conditions Eq. (9) (black solid curve), the function e^{kz} (crosses), the function e^{2kz}
 326 (dashed line). The panels (a)-(j) corresponds to the experiments No. 1, 3, 5, 7, 9, 11, 13-15, 18
 327 respectively, the panel (k) corresponds to the experiments No. 21-27.

328

329

330
$$(\omega - U_w(\mathbf{0})k)^2 \frac{d\Psi_1(\mathbf{0})}{dz} + (\omega - U_w(\mathbf{0})k)k\Psi_1(\mathbf{0}) \frac{dU_w(\mathbf{0})}{dz} - k^2 g\Psi_1(\mathbf{0}) = 0, \quad (14)$$

331

$$\Psi_1 \Big|_{z \rightarrow -\infty} \rightarrow 0.$$

332 Numerically solving the boundary layer problem for Eq. (11) (13) with the boundary
 333 conditions in Eq. (12) (14) enables one to obtain the dispersion relation $\omega(k)$ for the
 334 surface waves at the inhomogeneous shear flow. Note that because the phase velocity of
 335 the waves significantly exceeded the flow velocity in all experiments (cf. Figs. 2 and 3),
 336 the Rayleigh equation did not have a singularity, and the calculated frequency and phase
 337 velocity of the wave were real values, i.e., the current was neutral stable.

338 The wave phase velocities $C_{S\text{-theor-1}} = \omega(k)/k$ were calculated for the parameters of
 339 those experiments that contained complete information about the course and
 340 characteristics of the waves, namely 1, 3, 5, 7, 9, 11, 13–15, 18, and 21–27 from Table 1.
 341 The results are presented in Fig. 7a as the measured phase velocity C_s versus calculated
 342 phase velocity $C_{S\text{-theor-1}}$. One can see that the model corresponds to the data substantially

343 better than does the model of linear potential waves at the homogeneous current U_{BULK}
 344 (compare Fig. 6b). Considering the structure of the wave disturbances of the stream
 345 function, $\Psi_1(z)$, which was found as the eigenfunction of the boundary problem of Eqs.
 346 (11, 12). The profiles of $\Psi_1(z)$ are presented in Fig. 8. One can see that in all cases the
 347 functions $\Psi_1(z)$ are close to e^{kz} at the background of the mean velocity profiles. Moreover,
 348 for experiments No. 1, 3, 5, 15, and 21–27 (see Fig. 8a, 8b, 8c, 8i, and 8k), the wave field
 349 is concentrated near the surface at a distance less than the scale of the change in the mean
 350 flow, where the flow velocity is approximately equal to U_{SURF} . This explains the good
 351 correlation in these cases of the observed phase velocity with the phase velocity of waves
 352 at the homogeneous current U_{SURF} presented in Fig. 6a. At the same time, for experiments
 353 No. 7, 9, 5, 11, 13, 14, and 18 (see Figs. 8d–8h, and 8j), the scale of the variability of the
 354 flow is significantly smaller than the scale of the wave field. Under these conditions, a
 355 significant difference between the phase velocity of the waves and that given by the linear
 356 dispersion relation can be due to the influence of nonlinearity.

357 To estimate the nonlinear addition to the wave phase velocity, we used the results
 358 of the weakly nonlinear theory of surface waves for the current with a constant shear. Of
 359 course, the flow in the experiments of the present work does not have a constant shift, and
 360 this was considered when obtaining the linear dispersion relation. However, it should be
 361 taken into account that the contributions of the n -th harmonic to the nonlinear dispersion
 362 relation are determined by wave fields in the n -power, which have a scale that is n time
 363 smaller than the first harmonic. Additionally, the model of constant shear of the mean
 364 current velocity is already approximately applicable for the 2nd harmonic (see Fig. 8).

365 We use the nonlinear dispersion relation for waves in the current with a constant
 366 shift in the deep-water approximation, which was obtained by Simmen and Saffman
 367 (1985):

$$\begin{aligned}
 368 \quad & (\omega - U_w(0)k)^2 \frac{d\Psi_1(0)}{dz} + (\omega - U_w(0)k)k\Psi_1(0) \frac{dU_w(0)}{dz} - k^2 g\Psi_1(0) = \gamma(ka)^2, \\
 369 \quad & \gamma = \frac{(\omega_0 - U_w(0)k)^2}{2k} \left(1 - \frac{1}{2}\Omega^2 + \left(1 + 2\Omega + \frac{1}{2}\Omega^2 \right)^2 \right), \\
 370 \quad & \Omega = \frac{1}{(\omega_0 - U_w(0)k)} \frac{dU_w(0)}{dz},
 \end{aligned} \tag{15}$$

371 Here, ω_0 is the solution of the linear dispersion equation. Eq. ~~(13)~~ (15) is rewritten in the
 372 notation of this work and formulated in a reference frame in which the surface of the
 373 water has the velocity $U_w(0)$. Note that the linear part of Eq. ~~(13)~~ (15) coincides with Eq.
 374 ~~(12)~~ (14). The results of solving Eq. ~~(13)~~ (15) are presented in Fig. 7b similarly to Fig. 7a
 375 as the measured phase velocity C_s versus calculated phase velocity $C_{s\text{-theor-nl}} = \omega(k)/k$,

376 where one can see their good agreement with each other. Thus, the wave frequency shift
377 can be explained by two factors, including the Doppler shift at the mean flow and the
378 nonlinear frequency shift, while, the latter can also be interpreted in its physical nature as
379 the wave frequency shift in the presence of its orbital velocities.

380 Recent studies have indicated a regime shift in the momentum, heat, and mass
381 transfer across an intensive broken wave surface along with the amount of dispersed
382 droplets and entrained bubbles at extreme high wind speeds over 30 m s^{-1} (e.g., Powell et
383 al., 2003; Donelan et al., 2004; Takagaki et al., 2012, 2016; Troitskaya et al., 2012; Iwano
384 et al., 2013; Krall and Jähne, 2014; Komori et al., 2018; Krall et al., 2019). Thus, there is
385 the possibility of a similar regime shift in the Doppler shift of wind waves by the current
386 at extreme high wind speeds. However, the present study reveals that such a Doppler shift
387 is observed as under the conditions of normal wind speeds. In this case, the weakly
388 nonlinear approximation turns out to be applicable for describing the dispersion
389 properties of not only small-amplitude waves but also nonlinear and even breaking waves.
390 This implies that the intensive wave breaking at extreme high wind speeds occurs with
391 the saturation (or dumping) of the wave height rather than the wavelength. This evidence
392 might be helpful in investigating and modelling the wind-wave development at extreme
393 high wind speeds.

394

395 **4. Conclusion**

396 The effects of the current on wind waves were investigated through laboratory
397 experiments in three different wind-wave tanks ~~along~~ with a pump at Kyoto University,
398 Japan, Kindai University, Japan, and IAP RAS. ~~In this experiment, 27 different types of~~
399 ~~currents were generated at wind speeds ranging from 7 to 67 m s⁻¹. The study investigated~~
400 ~~27 cases with carrying winds, waves, and currents, at wind speeds ranging from 7–67 m~~
401 ~~s⁻¹. We observed that the wind waves do not follow the dispersion relation in either the~~
402 ~~normal or the extremely high wind speeds in the three tanks (Fig. 4)—excluding case 25,~~
403 ~~in which the artificial current experiment used the Kindai tank. In case 25, U_{SURF} is~~
404 ~~approximately zero (Fig. 3); thus, the Doppler shift does not occur. Then, using 18~~
405 ~~datasets (Kyoto and IAP RAS tanks) (Fig. 5), we found that the ratio of C_S/C_{S,0} is constant~~
406 ~~at both normal and extremely high wind speeds. Moreover, in the artificial current~~
407 ~~experiment in Kindai, we observed that the ratio varies (Fig. 5). The evidence from the~~
408 ~~three tank experiments implies that the same wave-current interaction occurs at normal~~
409 ~~and extremely high wind speeds.~~

410 ~~To develop an adequate model for wave-current interaction at normal and~~
411 ~~extremely high wind speeds, we validated four models (Figs. 6 and 7). At normal wind~~

412 speeds under 30 m s^{-1} , the wave frequency, wavelength, phase velocity of waves, and
413 surface velocity of the water ~~depended were found to depend~~ on the wind speed (Fig. 3).
414 However, the bulk velocity of the water showed a dependence on the tank type, i.e., ~~open~~
415 ~~tank~~ a large tank with a submerged wind-wave flume (IAP RAS) or ~~closed-tank wind~~
416 flume above a tank (general type of wind-wave tank) (Kyoto University) (Fig. 3). The
417 effect of the Doppler shift was confirmed at normal wind speeds, i.e., the significant
418 waves were accelerated by the surface flow, and the phase velocity was represented as the
419 sum of the surface velocity of water and the phase velocity, which is estimated by the
420 dispersion relation of the deep-water waves (Fig. 6). At extreme high wind speeds over 30
421 m s^{-1} , a Doppler shift was observed similar to that under the conditions of normal wind
422 speeds (Figs. 4 and 5). This suggests that the Doppler shift is an adequate model for
423 representing the acceleration of wind waves by the current, not only for the wind waves at
424 normal wind speeds but also for those with intensive breaking at extreme high wind
425 speeds. The data obtained by the artificial current experiments conducted at Kindai
426 University were used to explain how the artificial current accelerates (or decelerates) the
427 significant waves. A weakly nonlinear model of surface waves at a shear flow was
428 developed (Fig. 7). It was shown that it describes well the dispersion properties of not
429 only small-amplitude waves but also strongly nonlinear and even breaking waves, typical
430 for extreme wind conditions, with speeds, U_{10} , exceeding 30 m s^{-1} .

431

432

433

Data availability

434 All analytical data used in this study are compiled in Table 1.

435

436

Author contributions

437 NT and NS planned the experiments, evaluated the data, and contributed equally to
438 writing the paper excluding Section 3.2. YT planed the Russia experiment, provided the
439 linear and non-linear models, prepared figures in Section 3.2, and contributed to writing
440 Section 3.2. CT prepared all figures excluding Section 3.2. NT performed the wind,
441 current, and wave measurements in the Kyoto experiment. NT, NS, and CT performed the
442 wind, current, and wave measurements in the Kindai experiment. AK and MV performed
443 the wind, current, and wave measurements in the Russia experiment.

444

445

Competing interests

446 The authors declare that they have no conflict of interest.

447

Acknowledgements

This work was supported by the Ministry of Education, Culture, Sports, Science and Technology (Grant-in-Aid No's. 18H01284, 18K03953, and 19KK0087). ~~This project was supported by the Japan Society for the Promotion of Science and the Russian Foundation for Basic Research under the Japan Russia Research Cooperative Program.~~ This project was supported by the Japan Society for the Promotion of Science and the Russian Foundation for Basic Research (grant 18-55-50005, 19-05-00249, 20-05-00322) under the Japan-Russia Research Cooperative Program. The experiments of IAP RAS were partially supported by RSF (project 19-17-00209). We thank Prof. S. Komori and Mr. Tsuji for their help in conducting the experiments and for useful discussions. The experiments of IAP RAS were performed at the Unique Scientific Facility "Complex of Large-Scale Geophysical Facilities" (<http://www.ckp-rf.ru/usu/77738/>).

Appendix

It is important to estimate the phase velocity and wavelength of the significant wind-waves using the water-level fluctuation data. Here, we explain the method, called as the cross-spectrum method. The water-level fluctuation $\eta(x, t)$ at arbitral location x and time t is shown as the equation:

$$\eta(x, t) = \int_{-\Omega}^{\Omega} A(\omega) e^{i(\omega t - k(\omega)x)} d\omega \quad (\text{A1})$$

where ω is the angular frequency, $A(\omega)$ is the complex amplitude, and $k(\omega)$ is the wavenumber of waves having ω , Ω is the maximum angular frequency of the surface waves. $F_{\eta}(\omega)$ is the Fourier transformation of $\eta(x, t)$ when the measurement time t_m and Ω are sufficiently large. Using the inverse Fourier transformation of $F_{\eta}(\omega)$, $\eta(x, t)$ is shown as:

$$\eta(x, t) = \frac{1}{2\pi} \int_{-\Omega}^{\Omega} F_{\eta}(\omega) e^{i\omega t} d\omega. \quad (\text{A2})$$

Comparing Eqs. (A1, A2), $F_{\eta}(\omega)$ is $F_{\eta}(\omega) = 2\pi A(\omega) e^{-ik(\omega)x}$. Assuming that the wind waves change the shape little between two wave probes set upstream and downstream, we can set the upstream and downstream water-level fluctuations $\eta_1(t) = \eta(0, t)$ and $\eta_2(t) = \eta(\Delta x, t)$, respectively, with Δx downstream from the first probe. The Fourier transformations $F_{\eta_1}(\omega)$ and $F_{\eta_2}(\omega)$ for $\eta_1(t)$ and $\eta_2(t)$, respectively, are shown as:

$$F_{\eta_1}(\omega) = 2\pi A(\omega), \quad (\text{A3})$$

$$F_{\eta_2}(\omega) = 2\pi A(\omega) e^{-ik(\omega)\Delta x}. \quad (\text{A4})$$

Then, the power spectra $S_{\eta_1\eta_1}(\omega)$ and $S_{\eta_2\eta_2}(\omega)$ for $\eta_1(t)$ and $\eta_2(t)$, respectively, are shown

482 as:

$$S_{\eta_1\eta_1}(\omega) = \frac{1}{t_m} F_{\eta_1}^*(\omega) F_{\eta_1}(\omega) = \frac{1}{t_m} 4\pi^2 |A(\omega)|^2, \quad (A5)$$

483

$$S_{\eta_2\eta_2}(\omega) = \frac{1}{t_m} F_{\eta_2}^*(\omega) F_{\eta_2}(\omega) = S_{\eta_1\eta_1}(\omega). \quad (A6)$$

484

485 Here, the superscript * indicates the complex conjugate number. The cross-spectrum
 486 $Cr(\omega)$ for $\eta_1(t)$ and $\eta_2(t)$ is shown as:

$$Cr(\omega) = \frac{1}{t_m} F_{\eta_1}^*(\omega) F_{\eta_2}(\omega) = \frac{1}{t_m} 4\pi^2 |A(\omega)|^2 e^{ik(\omega)\Delta x}. \quad (A7)$$

487

488 Using Euler's theorem, Eq. (A7) transforms to:

$$\begin{aligned} Cr(\omega) &= \frac{1}{t_m} 4\pi^2 |A(\omega)|^2 (\cos k(\omega)\Delta x + i \sin k(\omega)\Delta x) \\ &= S_{\eta_1}(\omega) (\cos k(\omega)\Delta x + i \sin k(\omega)\Delta x). \end{aligned} \quad (A8)$$

489

490

491 The cospectrum $Co(\omega)$ and quad spectrum $Q(\omega)$ are defined as the real and imaginary
 492 parts of $Cr(\omega)$, respectively, shown as $Cr(\omega) = Co(\omega) + iQ(\omega)$. Moreover, the phase $\theta(\omega)$
 493 is defined as $\theta(\omega) = \tan^{-1}(Q(\omega)/Co(\omega))$. Thus, $\theta(\omega)$ can be calculated as:

$$\theta(\omega) = \tan^{-1}(\tan(k(\omega)\Delta x) = k(\omega)\Delta x. \quad (A9)$$

494

495 Generally, the velocity of the wind waves C is defined as:

$$C = \frac{\omega}{k} = \frac{L}{T}, \quad (A10)$$

496

497 where L is the wavelength and T is the wave period. From Eqs. (A9, A10), $C(\omega)$ and $L(\omega)$
 498 can be transformed to

$$C(\omega) = \frac{\omega}{k} = \frac{\omega\Delta x}{\theta(\omega)}, \quad (A11)$$

499

$$L(\omega) = \frac{2\pi}{k} = \frac{2\pi\Delta x}{\theta(\omega)}. \quad (A12)$$

500

501 When we estimate the phase $\theta_m(\omega_m)$ at the angular frequency of significant wind-waves
 502 $\omega_m (=2\pi f_m)$, the phase velocity of the significant wind waves $C_s (=C(\omega_m))$ and significant
 503 wavelength $L_s (=L(\omega_m))$ are calculated by:

$$C_s = \frac{2\pi f_m \Delta x}{\theta(f_m)}, \quad (A13)$$

504

$$L_s = \frac{2\pi\Delta x}{\theta(f_m)}. \quad (A14)$$

505

506 In the study, C_s and L_s are estimated by Eqs. (A13, A14) using the cross-spectrum

507 [method.](#)

508

509

510

References

511 Dawe, J. T., Thompson, L., (2006), Effect of ocean surface currents on wind stress, heat
512 flux, and wind power input to the ocean, *Geophysical Research Letters*, 33, L09604,
513 doi:10.1029/2006GL025784

514 Donelan, M.A., Haus, B.K., Reul, N., Plant, W.J., Stiassnie, M., Graber, H.C., Brown,
515 O.B., Saltzman, E.S., (2004), On the limiting aerodynamic roughness of the ocean
516 in very strong winds, *Geophysical Research Letters*, 31,
517 doi:10.1029/2004GL019460. L18306

518 Fan, Y., Ginis, I., Hara, T., (2009), The Effect of Wind–Wave–Current Interaction on
519 Air–Sea Momentum Fluxes and Ocean Response in Tropical Cyclones, *Journal of*
520 *Physical Oceanography*, 39, pp. 1019-1034.

521 Iwano, K., Takagaki, N., Kurose, R., Komori, S., (2013), Mass transfer velocity across
522 the breaking air-water interface at extremely high wind speeds, *Tellus B* 65, 21341,
523 doi:10.3402/tellusb.v65i0.21341

524 Kara, A. B., Metzger, E. J., Bourassa, M. A., (2007), Ocean current and wave effects on
525 wind stress drag coefficient over the global ocean, *Geophysical Research Letters*,
526 34, L01604, doi:10.1029/2006GL027849

527 Kawabe, M., (1988), Variability of Kuroshio velocity assessed from the sea-level
528 difference between Naze and Nishinoomote, *Journal of oceanographical Society of*
529 *Japan*, 44, pp. 293-304.

530 Kelly, K. A., Dickinson, S., McPhaden, M. J., Johnson, G. C., (2001), Ocean currents
531 evident in satellite wind data, *Geophysical Research Letters*, 28(12), pp.
532 2469-2472.

533 Komori, S., Iwano, K., Takagaki, N., Onishi, R., Kurose, R., Takahashi, K., Suzuki, N.,
534 (2018), Laboratory measurements of heat transfer and drag coefficients at
535 extremely high wind speeds, *Journal of Physical Oceanography*,
536 doi:10.1175/JPO-D-17-0243.1

537 Krall, K. E., Jähne, B., (2014), First laboratory study of air-sea gas exchange at hurricane
538 wind speeds, *Ocean Science*, 10(2), 257-265, doi:10.5194/os-10-257-2014

539 Krall, K. E., Smith, A. W., Takagaki, N., Jähne, B., (2019), Air–sea gas exchange at wind
540 speeds up to 85 m s⁻¹, *Ocean Science*, 15(6), doi: 10.5194/os-15-1783-2019

541 Powell, M. D., Vickery, P. J., Reinhold, T. A., (2003), Reduced drag coefficient for high
542 wind speeds in tropical cyclones, *Nature*, 422, 279–283, doi:10.1038/nature01481

- 543 Shi, Q., Bourassa, M. A., (2019), Coupling Ocean Currents and Waves with Wind Stress
544 over the Gulf Stream, *Remote Sensing*, 11, 1476, doi:10.3390/rs11121476
- 545 Simmen, J. A., Saffman, P. G., (1985), Steady deep-water waves on a linear shear current,
546 *Studies in Applied Mathematics*, 73, 35–57, doi: 10.1002/sapm198573135
- 547 Takagaki, N., Komori, S., Suzuki, N., Iwano, K., Kuramoto, T., Shimada, S., Kurose, R.,
548 Takahashi, K., (2012), Strong correlation between the drag coefficient and the
549 shape of the wind sea spectrum over a broad range of wind speeds, *Geophysical*
550 *Research Letters*, 39, doi:10.1029/2012GL053988. L23604
- 551 Takagaki, N., Komori, S., Suzuki, N., Iwano, K., Kurose, R., (2016), Mechanism of drag
552 coefficient saturation at strong wind speeds, *Geophysical Research Letters*, 43,
553 doi:10.1002/2016GL070666
- 554 Takagaki, N., Komori, S., Ishida, M., Iwano, K., Kurose, R., Suzuki, N., (2017),
555 Loop-type wave-generation method for generating wind waves under long-fetch
556 conditions, *Journal of Atmospheric Oceanic Technology*, 34(10), 2129–2139,
557 doi:10.1175/JTECH-D-17-0043.1
- 558 [Takagaki, N., Suzuki, N., Takahata, S., Kumamaru, H., \(2020\), Effects of air-side](#)
559 [freestream turbulence on development of wind waves, *Experiments in Fluids*, 61,](#)
560 [136, doi:10.1007/s00348-020-02977-9](#)
- 561 Troitskaya, Y. I., Sergeev, D. A., Kandaurov, A. A., Baidakov, G. A., Vdovin, M. A.,
562 Kazakov, V. I., (2012), Laboratory and theoretical modeling of air-sea momentum
563 transfer under severe wind conditions, *Journal of Geophysical Research*, 117,
564 C00J21, doi:10.1029/2011JC007778
- 565 [Troitskaya, Y., Sergeev, D., Vdovin, M., Kandaurov, A., Ermakova, O., Takagaki, N.,](#)
566 [\(2020\), Laboratory study of the effect of surface waves on heat and momentum](#)
567 [transfer at strong winds, *Journal of Geophysical Research Oceans*, doi:](#)
568 [10.1029/2020JC016276](#)
- 569
- 570